

LIQUID BRIDGE MODELING OF FLOATING ZONE PROCESSING *

by I. Martínez

Universidad Politécnica de Madrid
E.T.S.I.Aeronáuticos, 28040-Madrid, Spain

ABSTRACT

A simplified fluidmechanical interpretation of some silicon growth experiments performed aboard Spacelab-1 is given, using the capillary liquid bridge theory, which is discussed in depth. A model is developed to simulate the outer shape during the floating zone process performed, and ideas are given for a more complete thermal simulation. These models would help experimentalists in crystal growth and zone refining to predict unstable configurations, avoid bridge disruption and achieve the desired shape at every stage.

INTRODUCTION

A lot of the thermal processing techniques used in present-day materials technology are still full of empirism, and thus, clues to enhance their performances are most difficult to draw. The lack of a suitable theory that could set guidelines to further progress is due to poor understanding of the complex thermodynamic, physico-chemical and fluidmechanical phenomena that interplay.

In particular, the floating zone technique of rod refining and single-crystal growth has lately caught a lot of attention because of its outstanding importance in the manufacture of semiconductor materials of the highest purity for the expanding microelectronics and optoelectronics industries, when dislocation, impurities and other defects must be kept down to several parts in 10^{12} to reach integration levels higher than the present 10^9 junctions per cm^2 .

In this context, this paper presents a model that serves to explain some singular behaviour found during experimentation with melting rods of silicon in a microgravity environment, in particular predicting the evolution of the free molten interface. Equilibrium shapes and the stability of free interfaces and fusion- and solidification-fronts are key points to a controlled handling of molten zones.

*Based in the conference given in the ASI Summer School*at La Rábida and in Reference [27].

To put these developments on a better perspective, a preliminary review of the classical theory of thermodynamics of interfaces is presented, what will show up the need to perform experiments in reduced gravity to get large curved interfaces and make the experimental analysis easier.

A detailed study of static stability and energy evolution of axisymmetric liquid bridges is further developed as the most simple model of the complex real problem, considering several configurations of major interest where important results have been found.

In order to test the analytical and numerical models available, a wide-range experimental program is being pursued by this research team. On the one hand stays experimentation in a simulated microgravity environment [1] using Plateau's neutral buoyancy technique. On the other hand stays experimentation in real microgravity platforms: Spacelab-1 in 1983 [2], parabolic flights in NASA aircraft KC-135 and German sounding rocket TEXUS-10 in 1984, and TEXUS-12 [3] and Spacelab-D1 [4-7] in 1985. Results from these trials are also commented.

INTERFACES

Microgravity relevance

Most material systems appear as an ensemble of a few homogeneous bulk phases (solid, liquid or gaseous) with overall properties independent of the interface configuration. However, there are instances where interface effects play a dominant role, namely when volumetric forces become negligible ($\Delta\rho g L \ll \sigma/L$ for lengths L of interest) as in microgravity, and when the natural scale of the system (volume/interface area) is small. The latter refers to a finely divided heterogeneous mixture, as in colloidal systems (emulsions, foams, bubbling liquids, mists, etc), that are not considered here, despite its well-known importance.

Let us deepen in the analysis of why the microgravity environment is relevant to fluid science. Fluid science is an evolving subject that can be simply thought of as the conservation laws of physics applied to a local region of material (described by some constitutive equations) in local thermodynamic equilibrium, limited in space and time by appropriate initial and boundary conditions. At the atomic level, gravity is a weak volumetric force (10^{40} times smaller than the electrostatic one in the hydrogen atom and 10^{35} times in the molecule of hydrogen), but accumulates and becomes dominant when large masses are present, unless balanced by another body force. The main advantage that microgravity offers to fluid science is therefore the possibility of achieving large quiescent interfaces of uniform mean curvature, free from gradients of hydrostatic pressure, and showing high sensitivity to weak forces.

Experiments on Earth show many examples of capillary phenomena, but only in reduced dimensions (some millimeters) best characterized by the combination $\sqrt{\sigma/(\Delta\rho g)}$, known as capillary length, where σ is surface tension, $\Delta\rho$ is the density difference across the interface and g is gravity. It is important to notice that the material properties σ , $\Delta\rho$ and the contact angle θ (to be introduced later) are all independent of gravity. The spherical shape of small drops and bubbles, the colourful soap films, the varicosity and breaking of small jets, curved edges of all free surfaces, capillary rise and capillary pumping, retention of liquid in porous media, seepage on welding, displacement of a liquid by a more wetting one, flotation of ores by wetting agents, nucleation of drops and bubbles, and so on, are common examples.

The simplest system to be analyzed in microgravity is a large curved quiescent liquid/vapour interface of a pure substance with no external forces applied. From this basic configuration, extensions are made to include the effect of small additional perturbations: a constant residual acceleration, g-jitter, electrostatic and acoustic fields, and so on, although other possible perturbations as thermal, aerodynamic and electromagnetic fields are not contemplated here.

Under normal operating conditions, a neat division can be established between solid interfaces (where a solid and a fluid meet) and fluid interfaces (also called fluid/fluid interfaces) that may be liquid/liquid or liquid/gas. Their difference in mobility (solids retain their non-equilibrium shapes) renders their study widely apart, mainly because the diagnostic means are so distinct.

In what follows, the presence of a well defined fluid interface (that is, a heterogeneous system, and not a colloidal one) is always taken for granted, but in most instances a solid interface is also present. Thus, another useful classification is: interfaces without contact line and interfaces with contact line (further divided in: contact line without a solid and contact line with a solid, the latter being the most interesting). Several configurations of interest are presented in Fig. 1.

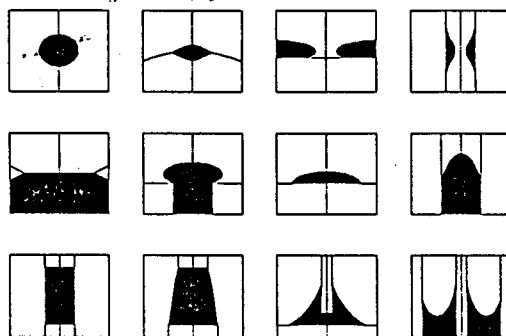


Fig. 1. Some axisymmetric fluid interface configurations of interest.

Another interesting classification from the point of view of materials science is: liquid-vapour, liquid-gas and liquid-liquid (immiscibles), for fluid interfaces, and liquid-solid, solid-vapour, solid-gas, solid-solid (grain boundaries) and solid-solid (distinct solids), for solid interfaces.

When two interfaces meet, a triple line exists that, if not anchored to a well defined edge, poses many problems both in practice (for positioning and handling) and in theory (for modeling the virtual displacements in stability studies).

Another remarkable thing to notice is that most of the methods to measure interfacial tension rely on the effect of gravity upon capillary systems, which rules them out in microgravity configurations as well as when the liquids are neutrally buoyant or near critical points.

But let us come back to the main point of characterizing interfaces. An interface is the region of high gradients in physicochemical properties where two volumetric phases meet. Under normal conditions, its thickness is only several molecular diameters wide. But one may wonder why do interfaces exist at all?, how is it in the interior?, and, from the practical point of view, how to treat them macroscopically. A simple one-dimensional model of phase transitions (where interfaces appear) gives

some insight to the first point.

Let a given number (large) of molecules be constrained to lay on a line, each one separated by its neighbours by a kind of spring, as illustrated in Fig. 2a. When the particles are widely separated, the spring model should approach the ideal gas pressure/volume relationship $F=k/d$, where F is force, d distance (spring length), and k a constant. When distances between particles are reduced (Fig. 2b) a kind of Lennard-Jones potential should be added that for one dimension gives $F=k/d-a/d^2+b/d^4$. This spring model is represented in Fig. 2f and reminds of van der Waals equation of state.

When the overall length (volume occupied by all the molecules) is reduced, first a proportional uniform reduction of all separations takes place (Fig. 2b), but if overall squeezing continues, spring span ceases to be uniform; some of them keep a length d_2 and some others adopt a length d_1 (Fig. 2c). Further overall distance reduction only increases the population of d_2 springs at the expenses of d_1 ones (Fig. 2d) until all of them are d_1 type and again a uniform shortening is brought by subsequent overall distance reduction.

Of course, this is just a qualitative model and do not explains the tendency to coalescence and other important observed behaviour of real interfaces.

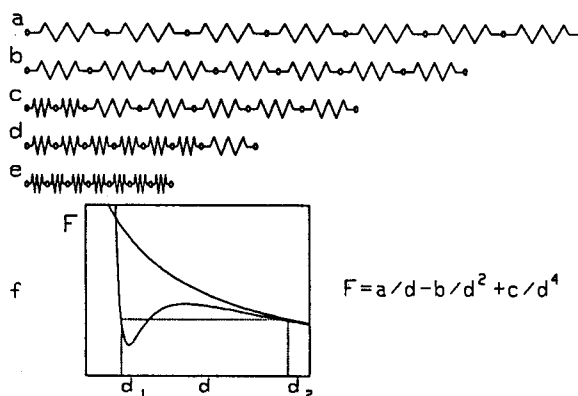


Fig. 2. A van-der-Waals-type of model for the occurrence of interfaces.

Fluid/fluid interfaces have great mobility, but solid/fluid interfaces lack it, their characteristic times are much longer and consequently they are normally under non-equilibrium conditions. Diffusion through interfaces and adsorption at them are vast subjects of research not dealt with here.

It is seen thence that interfaces appear as a consequence of thermodynamic instability, but why should interfaces have thermodynamic properties of their own and not be simply a geometrical surface separating two uniform different phases?

Microscopic and macroscopic views

Far from critical points the interface thickness is microscopic ($\sim 10^{-9}$ m), but if a macroscopic patch is considered ($> 10^{-7}$ m of side), the continuum model can be applied to microscopic distances along the normal to the interface, and thermodynamic functions drawn as in Fig. 3. The macroscopic approach is applied to get rid of these finer details and retain only what shows up at the larger scale. The traditional way (Gibbs 1878) is to

define a geometrical interface according to a certain criterion and extrapolate nearby bulk properties up to it (Fig. 3), assigning to this geometrical interface the excess value of the real physical properties and the extrapolated model. The usual criterion is to choose the interface at a location such that the excess density of one component vanishes. All interfaces have excess energy; besides, normal mixtures usually show excess concentration of solutes, but the contrary is the rule for electrolytic solutions. These excess properties are to be modeled by appropriate constitutive equations.

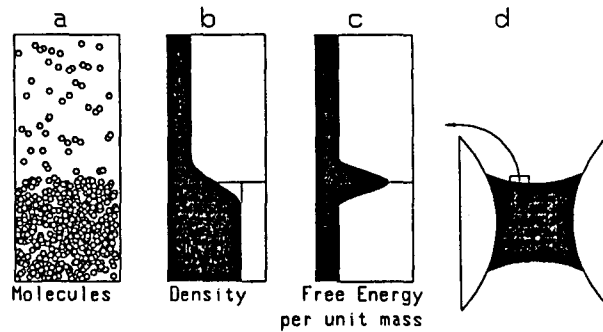


Fig. 3. Microscopic view of a liquid/vapor interface.

Because interfaces have excess energy, they tend to adopt a minimum area compatible with other constraints. To extend an interface under isothermal conditions a work $dW = \sigma \cdot dA$ must be done. For a pure substance σ only depends on temperature (pressure and temperature are coupled under phase transition), and has $d\sigma/dT < 0$ and $d^2\sigma/dT^2 > 0$. The internal energy per unit area, $U/A = \sigma - T \cdot d\sigma/dT$, varies in a similar way as the enthalpy of vaporization $h_{fg}(T)$, as shown in Fig. 4 for the case of water.

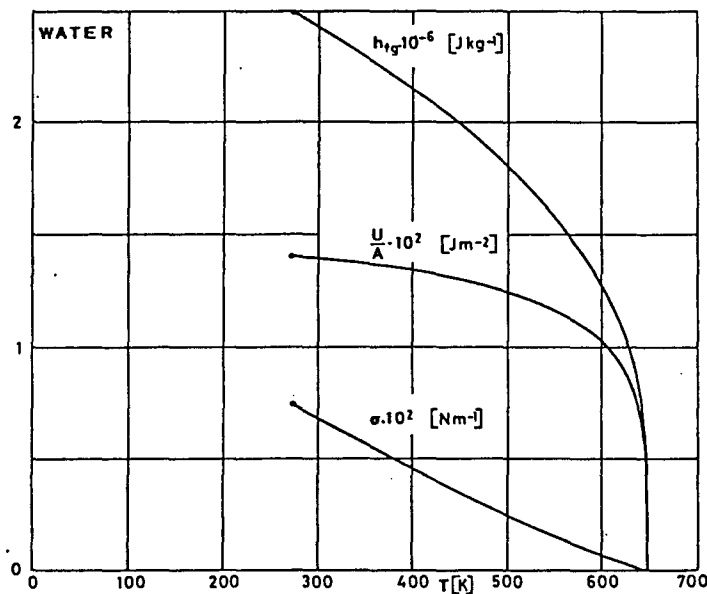


Fig. 4. The variation of surface energy U/A with temperature T is similar to the variation of the enthalpy of vaporization.

Between any two atoms or molecules, there is intermolecular attraction. Even in absence of net electrical charges, the electrons of each atom or molecule see and react to the motion of the electrons of all neighbouring molecules. The electrons arrange their motion accordingly, thus lowering the energy of the atomic entity. This correlated electron motion is the origin of van der Waals attraction and of surface tension. A molecule

looses the more potential energy the more molecules of the same species surround it, that is, there exists an energy of vaporization. A molecule moving from the liquid phase into the gas phase needs to gain this vaporization energy. It gains about half that energy (see Fig. 4) if it cannot join the vapour and instead constitutes part of the surface, where van der Waals attraction of one half of the molecules is still acting. This excess in energy of the surface molecules relative to the bulk cause the surface tension.

This statement on the surface tension of a liquid and the energy of vaporization apply in like manner to the interface tension between two liquids and the energy of mixing. Molecules of the same species generally exhibit a stronger van der Waals attraction than molecules of different species. It needs energy to exchange a molecule 1 within a drop of molecules 1 for a molecule 2. It needs loosely half this energy, if the two molecules are just brought to the interface between liquids 1 and 2. The molecules loose only about one half of the stronger attraction by the molecules of their own species.

Also, from investigations into the maximum possible undercooling rates one can conclude that the interface energy between a solid and its melt amounts to about one half of the energy of fusion. Similar relations hold between the mixing energy of two liquids exhibiting a miscibility gap and their interface tension. The interface tension vanishes at the critical point of the miscibility diagram. When the critical point is approached, one of the coexisting phases spreads along the surface of the liquid mixture and of the vessel.

Thermodynamics of interfaces

Consider a closed system composed of two fluid phases 1 and 2 with an interface s in between, in absence of any external force field. For the equilibrium of the whole system (phase 1, interface s and phase 2) the total entropy must be a maximum

$$S = S_1 + S_s + S_2 = \text{maximum} \quad (1)$$

subject to the constraints of constant volume V , energy U and amount of substance n_i

$$V = V_1 + 0 + V_2 = \text{constant} \quad (2)$$

$$U = U_1 + U_s + U_2 = \text{constant} \quad (3)$$

$$n_i = n_{i1} + n_{is} + n_{i2} = \text{constant for every specie } i \quad (4)$$

Substitution in Eq. (1) of $dS=(1/T)dU+(p/T)dV-\sum(\mu_i/T)dn_i$ for bulk phases and $dS=(1/T)dU-(\sigma/T)dA-\sum(\mu_i/T)dn_i$ for the interfacial phase, where μ_i is the chemical potential for the i -th specie, with Eqs. (2-4) yields

$$T_1 = T_s = T_2 \quad (5)$$

$$p_1 = p_2 + \sigma dA_s/dV_1 \quad (6)$$

$$\mu_{i1} = \mu_{is} = \mu_{i2} \quad \text{for every specie } i \quad (7)$$

where conditions of independence for the variations of U_1 , U_2 , n_{i1} , n_{i2} and V_1 (not those of V_2 and A_s , which depends on that of V_1), have been used.

Analytical geometry readily shows (first found by Gauss) that dA_s/dV_1 is the mean curvature C of the interface (the sum of the inverses of the principal radii of curvature, also equal to the divergence of the normal vector changed of sign). It is seen thence that thermodynamic equilibrium

requires constant temperature in all phases, a pressure jump across the interface proportional to local mean curvature (first stated by Young in 1804 and Laplace in 1805), and constant chemical potential throughout.

Introducing the surface concentration of component i , $\Gamma_i = dn_{is}/dA$, the Gibbs-Duhem equation for the interface phase (for unit area) is

$$0 = s_s dT_s + d\sigma + \sum \Gamma_i d\mu_{is} \quad (8)$$

which, in the limit of isothermal dilute solutions (chemical potential proportional to the logarithm of concentrations c) yields

$$\Gamma_i = \frac{-1}{RT} \frac{\partial \sigma}{\partial \ln c_i} \quad (\text{for dilute solutions}) \quad (9)$$

showing that, under isothermal conditions, the variation of surface tension with solutal concentration (proportional to μ_i) is opposed to adsorption, thus, in normal solutions whose components tend to be adsorbed at the interface, the interface tension diminish, whereas in electrolytic solutions with an interface depleted of solutes, the surface tension increases.

However, under normal circumstances the diffusive process that tends to equalize μ_i has a characteristic time much longer than the mechanical process involved in adjusting the pressure field, as happens with thermal processes. Thus, from now on, the influence of the concentration field will be neglected. In other words, equilibrium at T and V constant is reached when the Helmholtz free energy $F=U-TS$ has a minimum. As $F=\sigma A$, equilibrium implies minimum area, as already mentioned and, if there are several interfaces present, $F=\sum \sigma_i A_i$ must be a minimum. For a configuration as in Fig. 3d, because the area of solid interface is always constant, it suffices that the effective area

$$A_{\text{eff}} = A_{12} - A_{13} \cos \theta \quad (10)$$

be a minimum, for constant volume of bulk phases. If gravitational potential energy and rotation kinetic energy are included, the free energy F of the system is

$$F = \sum \sigma_i A_i + mgz_{\text{com}} - (1/2)I\omega^2 \quad (11)$$

where m is mass, g gravity, z_{com} center-of-mass height, I moment of inertia and ω rotation rate. Equilibrium requires $dF=0$ (with constant V) and stability requires $d^2F > 0$ (with constant V).

SHAPES AND STABILITY

In the previous paragraphs a thermodynamic approach was followed to arrive at the formulation of equilibrium and stability conditions of an interface. Now, a purely mechanical presentation is made to give a different perspective.

Isothermal fluid static configurations satisfy the mechanical equilibrium condition

$$\nabla(p+U)=0 \quad \text{at the bulk} \quad (12)$$

where ∇ stands for gradient, p is pressure and U the potential function of a possibly acting body force field. The boundary conditions are (Young-Laplace formulation)

$$\text{and } p^+ - p^- = \sigma \cdot C \quad \text{at an interface} \quad (13)$$

$$\sin\theta_1 / \sigma_{23} = \sin\theta_2 / \sigma_{13} = \sin\theta_3 / \sigma_{12} \quad \text{at a triple line} \quad (14)$$

where $p^+ - p^-$ is the pressure jump across the interface, σ is interface tension, C is local mean curvature and θ is fluid contact angle (Fig. 5).

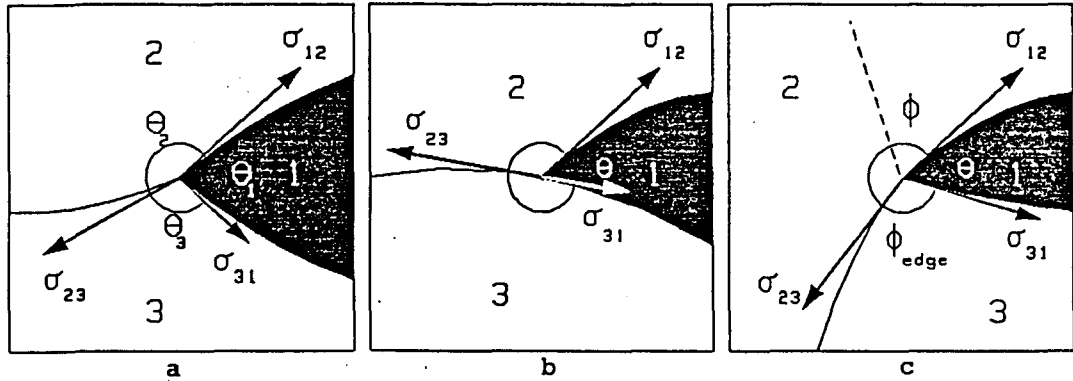


Fig. 5. Three typical contact-line configurations: a) at a three-fluid confluence, b) over a smooth solid, and c) anchored to a singularity (canthotaxis).

At thermodynamic equilibrium σ only depends on temperature for given substances. Although different liquid/liquid interfaces show wide variations in ρ , in liquid/gas interfaces it is only marginally sensitive to the nature of the gas. Similarly, contact angles also depend on temperature and composition of the three phases meeting, but, if one of them is gaseous, it shows little sensitivity to the gas composition.

Canthotaxis

A degenerate case of Eq. (14) happens when one of the phases is solid (see Fig. 5b). In such a case it takes the form

$$\sigma \cdot \cos\theta = \sigma_{23} - \sigma_{13} \quad (15)$$

Furthermore, if the solid surface presents a singularity at the three phase line, contact angle is irrelevant in the range of values

$$\theta < \phi < \pi - \phi_s + \theta \quad (16)$$

On the other hand, the local mean curvature of a surface is simply the divergence of the normal vector changed of sign

$$C = -\nabla \cdot \vec{n} \quad (17)$$

which can be found expanded in different coordinate systems (rectangular, cylindrical or spherical) in most textbooks on analytical geometry. In any case, the problem of finding equilibrium shapes reduces to solving the second order partial differential equation (13) with the pressure jump given by Eq. (12) at the interface, plus one of the boundary conditions (14)-(16), plus the condition of known fluid volume or feeding pressure (of course, it is quite different to consider stability at constant fluid volume that at constant feeding pressure).

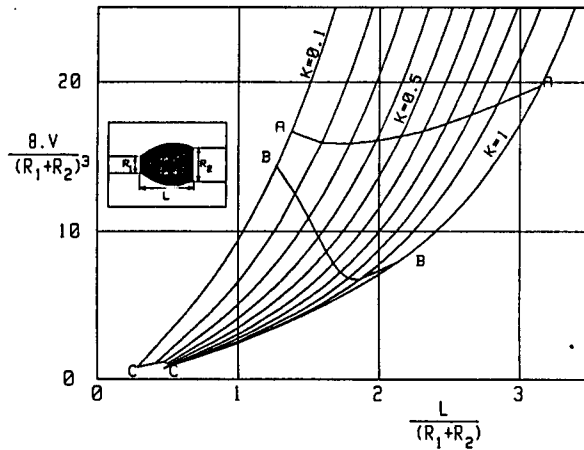


Fig 7. Stability limits for a floating zone of volume V , between unequal discs of radius R_1 and R_2 a distance L apart. The minimum stable volume for several disc ratio is shown. Curves AA, BB and CC correspond to bridges with minimum undulation, local cylindricality at the larger disc and catenoidal shapes, respectively.

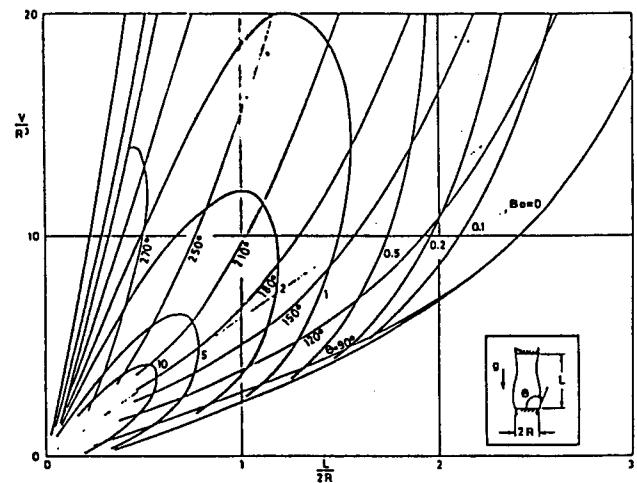


Fig 8. Stability limits for a floating zone of liquid volume V , held between equal discs of radius R a distance L apart, in the presence of an axial gravity field of acceleration g ($Bo = \rho g R^2 / \sigma$) [8].

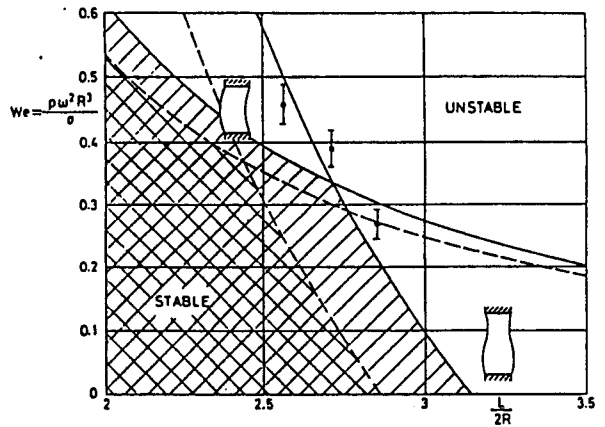


Fig 9. Critical rotation rates ω (solid lines) for cylindrical liquid bridges. Short bridges develop a C-mode deformation whereas bridges more slender than $L/(2R) = \frac{\pi}{2} \approx 1.57$ break in an amphora-like mode. The stable area is reduced (shown cross-hatched) if an axial gravity is present as during Spacelab-D1 trials. The three experimental points correspond to the three amphora-mode breakages in that flight.

response is analyzed (mainly the outer shape deformation). Aside of its own scientific relevance in fluid mechanics this work has many potential spinoff applications, as in the modeling of the floating zone technique used in materials science for the processing of semiconductors and high melting point materials, what is treated later in the paper.

The first microgravity experiments in this project were performed in Spacelab-1 (Dec-83) with only partial success because of uncontrolled liquid spreading beyond the edges of the supporting discs, which were protruding only 0.5 mm from their base plate. In spite of that, the resourceful crew managed to improvise new working discs and achieved large (although not cylindrical liquid columns, as the one shown in Fig. 10a, which corresponds to an isorotation sequence at 7 rpm with the column showing the long awaited C-mode deformation (like a skipping rope).

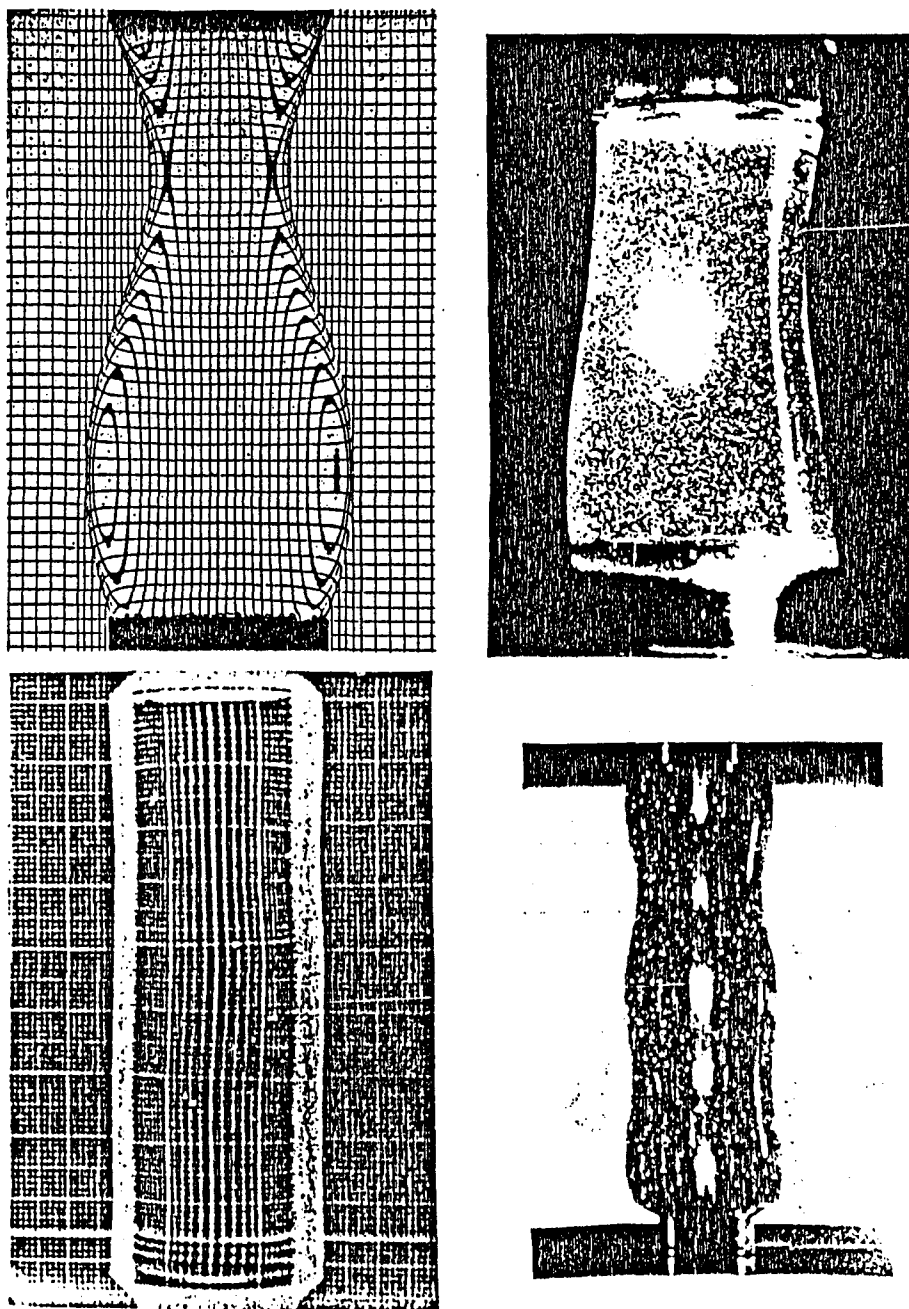


Fig. 10. Liquid columns obtained in different platforms: a) prior to rupture in a neutrally buoyant tank on the ground, b) C-mode deformation at 7 rpm in Spacelab-1, c) nearly perfect cylindrical zone in TEXUS-12, d) vibration at 1.1 Hz in Spacelab-D1.

In order to check the new disc design for the following Spacelab experiments, a series of parabolic flights with NASA KC-135 aircraft were flown in Dec-84, although the microgravity level achieved was too poor to handle large liquid masses.

Much better results were obtained on the TEXUS-12 rocket flight in May-85 (Fig. 11 shows the procedure followed), where perfect cylindrical liquid columns 82 mm long by 30 mm in diameter as the one shown in Fig. 10c were established (in a record time of about one minute). An earlier attempt in May-84 had been a complete failure due to equipment malfunction. A second campaign of parabolic flights were carried out in Jun-85 and again the ambient noise was too high to check Spacelab operations other than the necessary crew familiarization and training. These relatively cheap early trials may also serve to detect some materials incompatibility, as occurred indeed for other experiments, thus giving time to work out remedies and improving the reliability of multiuser facilities as the Fluid Physics Module used here.

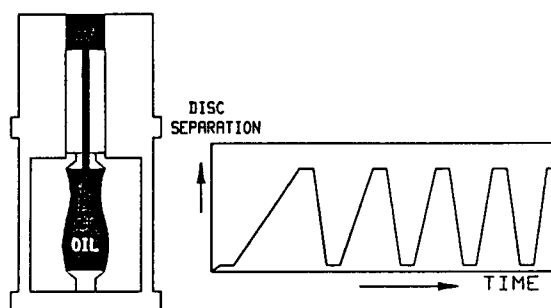


Fig. 11. Experiment in TEXUS-12 rocket. Movement of the upper disc assembly creates liquid columns as the one in Fig. 10c. Separation speed was increased until bridge disruption.

In November 1985, the sequence of Spacelab-1 trials were repeated aboard Spacelab-D1 with modified working discs and liquid injection system (Fig. 12) and this time everything run as foreseen. Payload Specialist Dr. Furrer was in charge of the experiment in flight, assisted by the investigator on ground when voice and video link was available. The experiment proceed as expected, with the following deviations:

- It was soon realized that the g-jitter effect was much more pronounced than Spacelab-1 and TEXUS-12 experience had shown. Long columns were continuously trembling.
- This noisy ambient stressed the operator, who on the first trial followed a slightly scarce filling law that caused the first disruption of the column soon after the nominal working length $L=95$ mm was reached.
- Experiment reinitialization was achieved thanks to the skillful operator (and not once but five times), demonstrating the importance of a well-trained Payload Specialist on board. During a real-time video link it was agreed to switch on background illumination to better follow the free surface oscillations (at expenses of a poorer tracer visualization by meridian plane lighting).
- The small rotation of the discs at 3 rpm, intended for overall viewing, was switched off to diminish ambient noise (work had to be stopped several times due to uncontrolled vibrations or Shuttle maneuvers).
- Axial oscillation of one disc at several frequencies was exercised and liquid response was as foreseen though departures from a cylinder were larger near the filling discs due to a residual acceleration. A second breaking took place just after the axial oscillation exercise due to a Shuttle maneuver.

- Further breakings occurred at $L=95$ mm with $\omega=12$ rpm, 100 mm with 10 rpm, and 90 mm with 13 rpm, all in an amphora-like mode. The last breaking showed an initial C-mode deformation (like a skipping rope), but ambient noise may have changed the final breaking mode.
- The last C-mode rotation trial, at $L=75$ mm with $\omega=16$ rpm, much less sensitive to ambient noise, was not performed due to lack of time, in spite of the generous time extensions granted to this experiment.

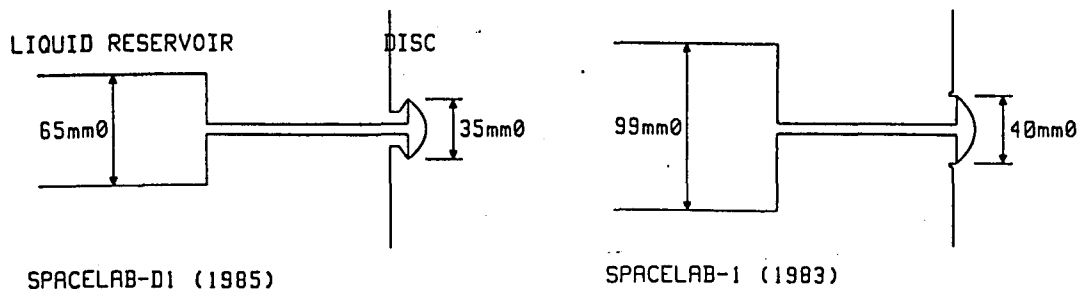


Fig. 12. Changes introduced in the working discs and the injection system.

The breaking of long cylindrical bridges has also been investigated by numerical simulation using a one-dimensional slice model [9]. The time evolution of the different energy terms (Fig. 13) gives a clear picture of the process. If some tracers are assumed to lay on the free surface, their respective paths may be traced with the model and can be seen in Fig. 14.

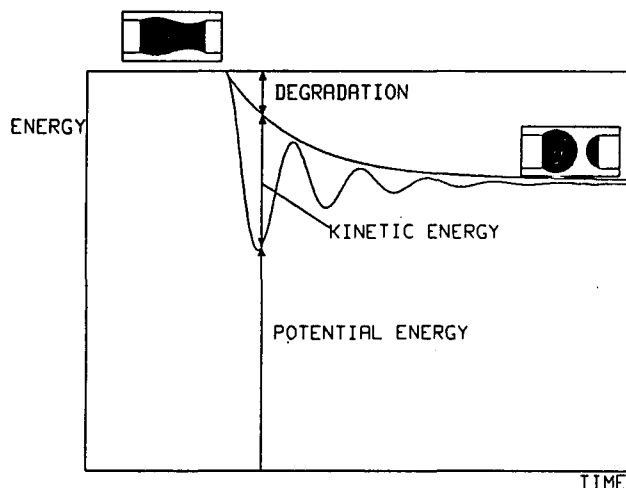


Fig. 13. Evolution of the free energy in a breaking bridge (an initially cylindrical column near the maximum stable length is slightly deformed to start the process).

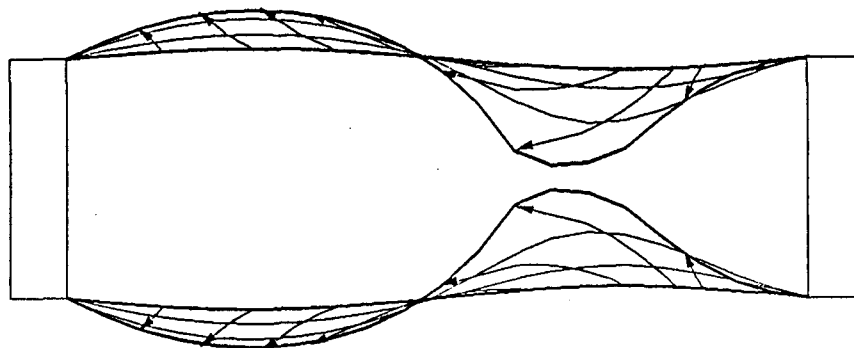


Fig. 14. Trajectory of surface tracers during the breaking of a bridge.

The most important result is the accurate prediction of the volume fraction of the two drops formed after bridge disruption, as shown in Ref. [5] for the experiments aboard Spacelab-D1 (a small free satellite drop is always observed in practice, but its volume is negligible).

CRYSTAL GROWTH

Introduction

Crystal growth is the aggregation of otherwise dispersed particles to an already existing solid lattice. This process demands some mobility of the particles, thence the disperse phase, although it may be a hot solid (recrystallization), is usually a fluid. Crystal growth from a gaseous phase is sometimes practiced (vapor growth techniques), as well as crystal growth from a cool liquid (solution growth techniques), but by far the largest quantity of materials is obtained by crystal growth from the melt.

This last technique is further classified according to the configuration of the three-phase contact line where the solid/melt interface meets the surrounding medium, that, although sometimes consisting of a solid wall or a molten salt, it is normally an inert gaseous atmosphere. Besides, three different configurations are usually distinguished: pulling a rod out of a molten bath (Czochralski technique), pulling a rod through a furnace (floating zone technique) or pushing a melt through a die (the most important of these being edge-defined film-fed growth). The latter seems to be the more versatile and is catching the market of semiconductor material production (mainly for solar cells), but the floating zone technique, the one dealt here, presents the advantage of the melt not being contaminated by the die or crucible materials and yields the purest materials.

It is important to realize that for crystal growth to occur the system needs to be in a non-equilibrium state, i.e. with a temperature (or concentration, or electric field, etc) gradient to provide the driving force, which must be very small to avoid instabilities at the solidification front (particularly constitutional supercooling). The decrease in entropy due to the ordering upon crystallization implies that heat must be removed from the sample.

Container-free floating-zone growth is a very common technique to get high purity crystals. The main advantage is that any contamination by the crucible material is avoided. Under gravity conditions, this method is used when the surface tension of the materials suffices to compensate the hydrostatic pressure in the melt. High vapor pressure of at least one of the components might prohibit this method, however.

To establish a floating zone, a relative motion between the sample rod to be processed and the furnace is imposed (Fig. 15), causing impurities to be swept to the rod ends by the difference in concentration at the melting and solidification fronts.

The interplay of thermodynamical, physicochemical and fluid-mechanical phenomena in this process is so entangled, that this technology is still full of empirism. Trying to better understand the underlying physics, a great effort is being devoted to the detailed study of more simple specific phenomena, both theoretically and experimentally. In particular, because one of the more conspicuous forces present is that of gravity, a proliferation of microgravity experiments has taken place since the availability of space platforms. Although some of them aim at obtaining new exotic materials, the majority are concerned with more fundamental

research, using well known materials, as for instance Experiment 1-ES-321 "Crystal growth of a silicon rod" performed aboard Spacelab-1 in Dec-83, which is the one to be analyzed here. But before that, let us have a look at the other important application of floating zones: materials purification.

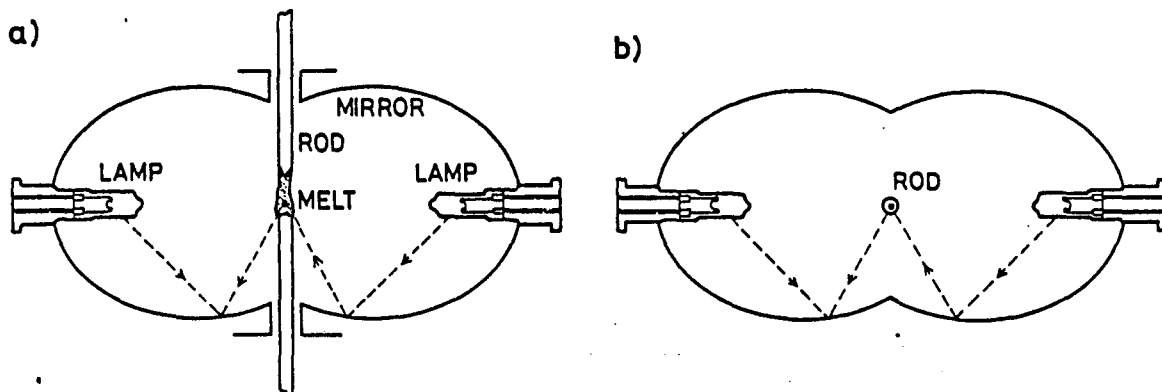


Fig. 15. Double ellipsoidal mirror furnace used in the crystal growth of silicon rods aboard Spacelab-1. a) side view, b) plant view.

Zone refining

Although the main interest of recent floating zone work is on growing single crystals, its first application [10] was in the purification of germanium for the (at that time) emerging solid-state industry. The floating-zone technique was developed from the well-known molten-zone technique, where the melt was supported on a crucible instead of by surface tension forces. It has been applied to low melting point materials (organic solids with $T_f \sim 300^\circ\text{C}$), medium temperatures (metals of $600 < T_f < 1000^\circ\text{C}$) and high melting point materials (some metals, its oxides and some other inorganic substances with $1000 < T_f < 2000^\circ\text{C}$). When the molten-zone technique was used, the crucible was a borosilicate glass or fused silica or platinum, according to the temperature ranges above mentioned. Sometimes the crucible was open to avoid problems of expansion and to have better access (to take out impurities).

The great advantage of crucible-free processing by the floating-zone technique is to get rid of thermal and solutal contamination, obtaining the purest man-made materials, with less than 1 ppm of impurities, that are needed not only for research but in the everdemanding microelectronics industry of today. Unfortunately, because of a large energy consumption and a small production rate, the cost of materials processed with this technique (less than 1 ppm impurities) rises to the order of 200 to 2000 \$/kg.

To establish a simple model of the zone refining process, the following simplifications are introduced:

- One-dimensional geometry (Fig. 16) instead of the real shape. All the important effects of shape stability are thus forgotten.

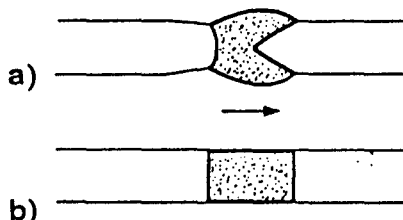


Fig. 16. Meridian section of a real floating zone, a), and the model, b).

-Negligible velocities for all interface fronts and internal motion in the liquid (due to Marangoni effects, diffusion, shrinking, etc).

Some other simplifications will be introduced later in the analysis, but let us see straight-on why impurities tend to segregate when the floating zone is made to travel.

A typical phase-equilibrium diagram for a roughly pure substance is shown in Fig. 17a, with the important example for silicon-aluminium in Fig. 17b. At constant pressure (the value is irrelevant for condense phases) the crucial point is that the solidus (SS' start of fusion) and liquidus (LL' start of solidification) lines are distinct.

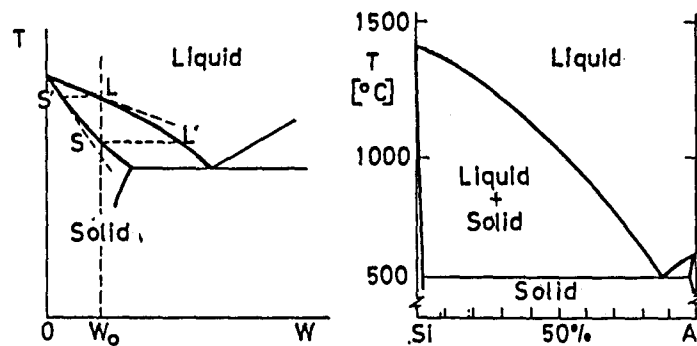


Fig. 17. a) Typical phase diagram for a binary mixture of high purity: (SS' solidus line, LL' liquidus line). b) Phase diagram for silicon-aluminium.

There are certain substances for which the slopes SS' and LL' are positive (as for phosphor in gallium arsenide), but the segregation due to the different affinity of every component in the different phase takes place anyway. The extreme case where the solidus line is vertical (the solid phase does not dissolve impurities, as in salt water) is a trivial case without interest here. Thus, when a liquid mixture with an impurity concentration W_0 starts to solidify (point L) the solid formed has a different concentration (point S'). Normally the solid phase is more pure and the remaining liquid (holding most of the impurities) is discarded. The model for zone refining is as follows: The initial condition is a solid rod of length Z_N with an impurity concentration profile $W_{g2}(Z)$, then a length (from the left) $Z=L(0)$ is melt, and afterwards the molten zone is made to travel to the right (forced by a relative movement of rod and heating device). At a generic instant we will have resolidified material from 0 to Z_1 , the melt from Z_1 to $Z_1+L(Z_1)$, and unprocessed material as left by the previous pass (Fig. 18).

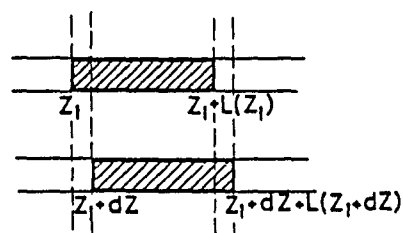


Fig. 18. Two successive instants in a zone refining process.

The following simplifications are introduced now:

- 1) Diffusivities inside the solid are neglected and thus composition cannot vary with time (except when resolidified)
- 2) Diffusivities inside the liquid are large, thus, in a first

approximation liquid composition is uniform

- 3) Thermodynamic equilibrium conditions apply to the solidification front Z_1 (and not to the melting front). That is, liquid and solid concentration of impurities are as in L and S' (Fig. 17a). For low impurity processing lines SS' and LL' may be approximated by their tangents at the origin $W=0$, thus

$$W_{s1}(Z_1) = k \cdot W_L(Z_1) \quad (18)$$

Where k is call the equilibrium segregation constant. A mass balance for impurities yields (see Fig. 3):

$$[W_L(Z_1) - W_{s1}(Z_1)]dz + [W_L(Z_1+dz) - W_L(Z_1)](L(Z_1) - dz) + \int_{Z_1+L(Z_1)}^{Z_1+dz+L(Z_1+dz)} [W_{s2}(z) - W_L(Z_1)]dz = 0 \quad (19)$$

What is wanted is to know the final concentration profile $W_{s1}(Z_1)$, that depends on the initial concentration profile $W_{s2}(Z_1)$, the molten zone law $L(Z_1)$ and the segregation constant k .

Equation (19) has analytical solutions in certain cases, as when $W_{s2} = \text{constant}$. If, in addition, $L(Z_1) = Z_N - Z_1$ (all the rest of the rod is molten) the solution is

$$\frac{W_{s1}(Z_N)}{W_{s2}} = k \left(\frac{Z_N - Z_1}{Z_N - Z_1} \right)^{1-k} \quad (20)$$

The above case serves to model the final solidification of a molten zone when the heating is removed (Fig. 19a). However, it presents a singular point at $Z_1 = Z_N$, showing that when the molten length shrinks to zero its impurity contents diverges because the solid takes less than the liquid offers (the model assumes small concentrations and ceases to be valid).

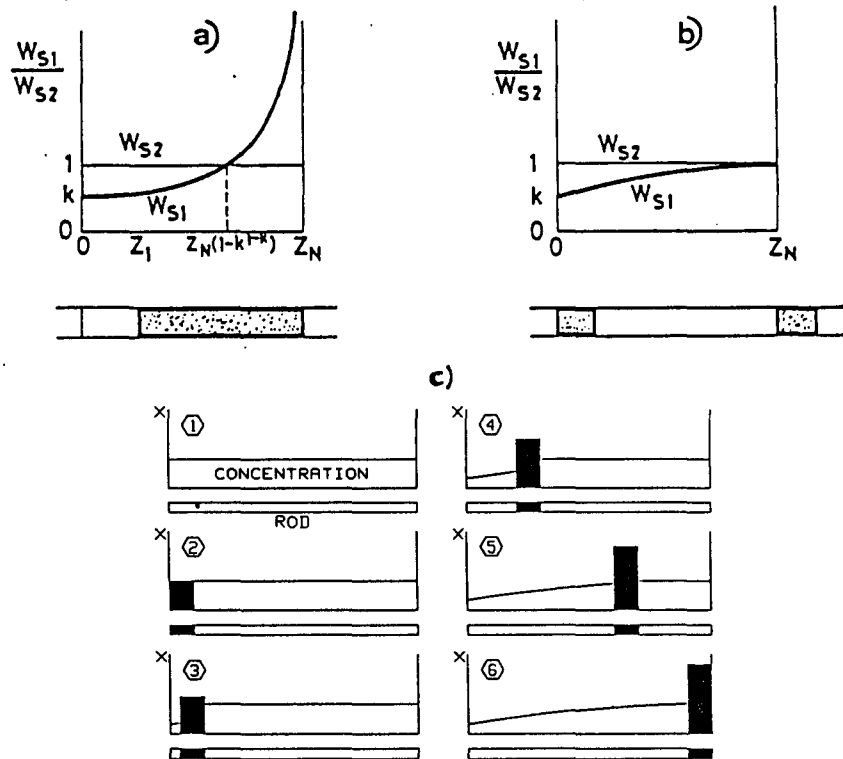


Fig. 19. Impurity concentration profile in a rod with an uniform initial concentration, after one processing pass. a) the full rod is molten and unidirectionally solidified, b) a constant length is molten and made to travel to the right, c) different time stages for case b).

Another interesting analytical solution with $W_{s2}=\text{constant}$ is obtained when $L(Z_1)=\text{constant}$ also (see Fig. 19b), yielding

The last solution serves to model the quasi-steady-state of the traveling zone. Note that, to represent a complete pass, this model must be combined with the former, at the right end, but if this part of the rod is to be discarded, the solution would be as in Fig. 19b.

In a more general case of $W_{s2}(Z)$, as for the second and following passes, recurs to numerical computations is necessary. From computer simulation with the above models, the following results can be obtained:

- The longest the molten zone, the best (limited in practice by shape instability)
- The initial rod should be as long as possible (at least 10 times the molten length) to avoid that the accumulated impurities at the end re-dissolve
- For the above reason, every pass should be slightly shorter than the previous one
- Also, the length of the molten zone should be reduced from pass to pass
- The purest material lies at the starting end
- The efficiency of passes decreases because the adverse concentration gradient forces some re-mixing
- After so many passes as molten-zone lengths has the initial rod (roughly) there is little benefit in re-processing.

Although all kinetic effects have been neglected, it implies that the pulling law for the molten zone has to be very small in practice (typically ~ 1 mm/min). If not, diffusion will be unable to homogenize the liquid phase (an effective segregation coefficient velocity-dependent could still be used) and finally the solidification front would destabilize and dendritic structures would develop.

Floating zone growth in Spacelab-1

The analysis presented here concerns the growth of two silicon crystals aboard Spacelab-1 (1983) in a so called Mirror Heating Facility [11], sketched in Fig. 15, developed explicitly for zone growth experiments in Spacelab-1, and tested on earth by numerous experiments yielding high quality crystals of different electronic materials (e.g. Si, CdTe, GaSb, InP) [12-14]. The radiation of two 400 W halogen lamps is focused on the sample by two adjoint ellipsoidal mirrors. Since the zone is heated by incoherent light, additional forces such as those existing for instance in RF heating are avoided. Thus, this method is specially suited to investigate the behaviour of free liquid bridges.

The furnace is moved over the sample, thus making the molten zone to travel through prefabricated silicon rods from bottom to top (Fig. 20). The special shape shown was chosen to achieve dislocation-free growth by starting the crystallization in the lower part of the thin neck. A detailed performance description is given in [15]. Figure 21 shows crystals grown using that furnace. In such radiation heated silicon growth experiments, the solid/liquid interface at the feed rod (upper interface in Fig. 20) tends to be cone-shaped, whereas the growing interface (bottom) is slightly convex [12-16].

Touching of the apex of the cone with the growing crystal has to be avoided in order to maintain monocrystalline structure. Even worse, if both solid ends are being counterrotated, the touching may cause

mechanical problems with the drives, and the melt may sputter over the furnace walls. That means that radiation power has to be high enough to exceed a minimal external length of the molten zone. But, on the other hand, an upper limit of this length also has to be attended in order to prevent liquid bridge disruption by capillary forces.

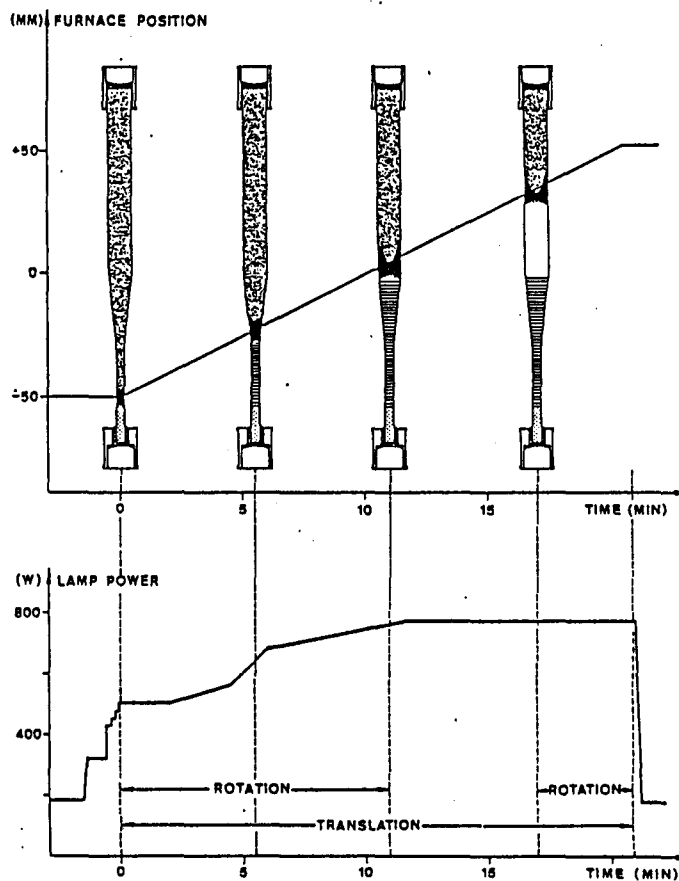


Fig. 20. Pulling and heating laws for Exp. 1-ES-321 aboard Spacelab-1.

There is a second critical problem aggravating floating zone growth under microgravity conditions. Surek and Chalmers [17] have shown that in silicon the angle between the meniscus of the melt and the growth direction (for constant cross-section growth) has to be 11° , i.e. the molten zone should bulge slightly outward of the growing interface. On the earth, the interaction between gravity and surface tension always cause the melt to broaden at the lower end so that the interface adopts an S-shape (see Fig. 22).

In space the situation is different. After establishing the liquid zone, its volume is, due to an 8% decrease in volume of Si upon melting, too small to form a cylindrical bridge, let alone an outward bulging surface. As a consequence, the diameter of the growing crystal will initially decrease until the melt attains a meniscus angle of 11° (see Fig. 23). This diameter reduction tends to be less pronounced and would eventually recover, since in steady state growth the amount of material melting must equal the amount crystallizing.

But this transient decrease in diameter may affect the stability of the zone. The margin of stable zone lengths thus becomes even smaller in microgravity than on earth, and a very skillful experimentation is required to steer clear from zone disruption on the one hand and of

solid/liquid interfaces touching on the other hand. This problem may be overcome in future by bringing the two solid ends (after a molten bridge is established) closer.

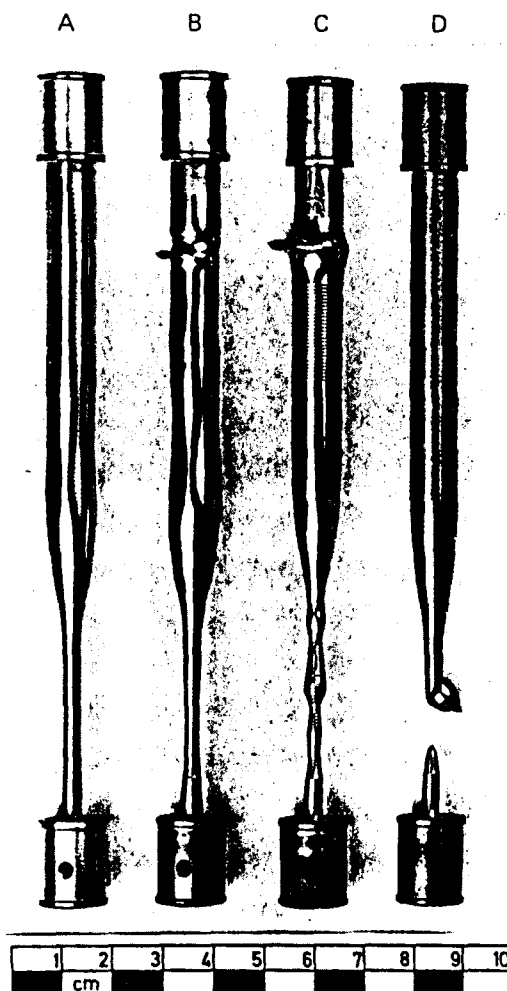


Fig. 21. Silicon rods: A) unprocessed, B) reference processed on ground, C) sample successfully processed in flight, D) sample processed in flight until bridge disruption occurred.

$T_F = 1685 \text{ K}$
 $\rho_L = 2520 \text{ kg/m}^3$
 $\rho_S = 2330 \text{ kg/m}^3$
 $\delta = 11^\circ$
 $\sigma = 0,75 \text{ N/m}$
 $k_L = 22 \text{ W/(mK)}$
 $k_S = 64 \text{ W/(mK)}$
 $h_F = 1,66 \cdot 10^6 \text{ J/kg}$
 $\epsilon_L = 0,64$

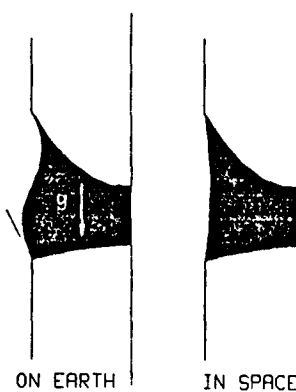


Fig. 22. Physical constants of silicon, and sketch of molten shapes (meridian section) when pulled on Earth and in space.

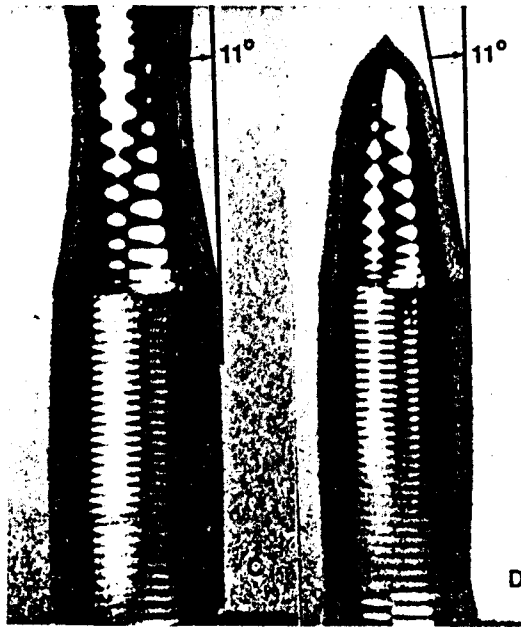


Fig. 23. Magnified view of the neck region for the two crystals processed in flight (Fig. 3C and 3D) showing the growth angle at start.

Rotation of the end supports is normally imposed to uniformize the heating. For instance, the furnace used here produced a two-lobed non-axisymmetrical radiation pattern. Fortunately, the rotation rates in use were so low that the influence on outer shape and stability limit seems negligible. Most of the sample, however, was grown without rotation, suffering the asymmetry of the radiation pattern.

Analysis of floating zone growth with the liquid bridge model

Two floating zone experiments were initiated during the Spacelab-1 mission. The first one took its scheduled course: a molten zone could be established in the neck and made to travel all the way to the end of the sample (Fig. 21C). There was video recording aboard and, during most of the time, TV transmission to the ground. The sequence of outer shapes of the melt was gathered from the video tapes and correlated with the crystals grown from these melts (Fig. 24). The irregularly shaped neck is the result of the difficulties encountered in adjusting by hand the proper zone length because of the meniscus problem mentioned above.

The second run had to be terminated shortly after starting of the zone travel because of rupture of the molten bridge (Fig. 22D shows the two pieces of that sample). Apparently, the zone length had become too large and the crystal diameter had decreased to such a degree that disruption near the lower interface occurred. The same occurrence had already taken place during a similar experiment in a sounding rocket [18].

A detailed view of the necks of the samples processed on board is presented in Fig. 23. The rotation rims appearing on the surface show that the samples were being rotated during growth. Crystal perfection evaluation, as well as a comparison of the earth grown and space grown crystals, concerning crystal structure, defect concentration and dopant distribution are reported elsewhere [15-16].

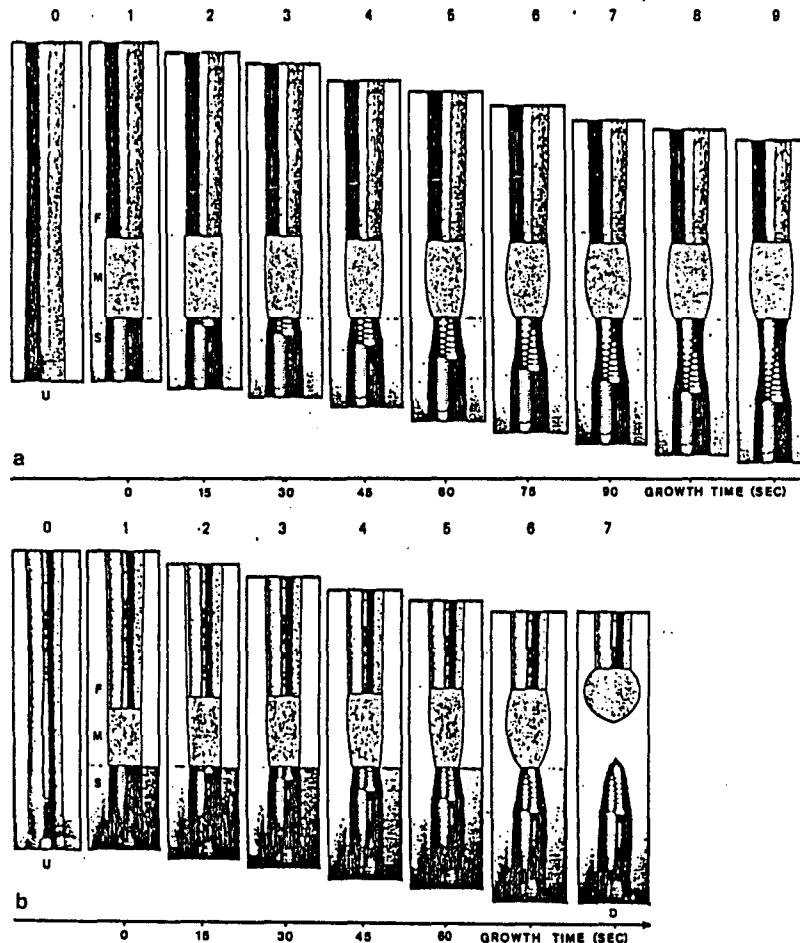


Fig. 24. Sequence of molten zones (depicted from video pictures). a) successful growth (Fig. 3C), b) bridge disruption in the second trial. U unmolten crystal, S seed crystal, M melt, F feed crystal. Note that shape D in b) immediately follows its previous picture; all others are 15 seconds apart.

What information can be gained by the experimenter with floating zones from the fluid-mechanical theory of liquid bridges? For instance, were the molten bridges equilibrium capillary menisci?, how far were they from capillary instability?. In all, what lessons from liquid bridge analysis can be advantageously used in crystal growth?

The fluid-mechanical behaviour of silicon floating zones can easily be explained by the simple liquid bridge theory of Laplace [19-26], provided the following simplifications are introduced:

- a) Axisymmetric geometry.
- b) Quasistatic configurations.
- c) Constant material properties.
- d) Negligible gravity, g-jitter and centrifugal effects.
- e) Deep melting (molten core).
- f) Free surface anchorage at both ends (seems to be quite realistic).

Under these hypothesis, the questions posed above may be answered as follows. Molten free surfaces at equilibrium should be part of a constant mean curvature surface (Plateau surface). They can be determined from three nondimensional parameters as, for instance, end diameter ratio H (see Fig. 25 for nomenclature), length divided by mean diameter Λ , and straight volume V (or neck to bulging ratio, what is easier to measure).

Although an explicit expression may be developed for small deviations from the cylinder, complicated graphical interpolation or involved computing are required in a general case. It should be noted, in any case, that in order to be able to detect deviations from equilibrium in real situations with small bridges (some millimeters in diameter), an accuracy of microns would be required.

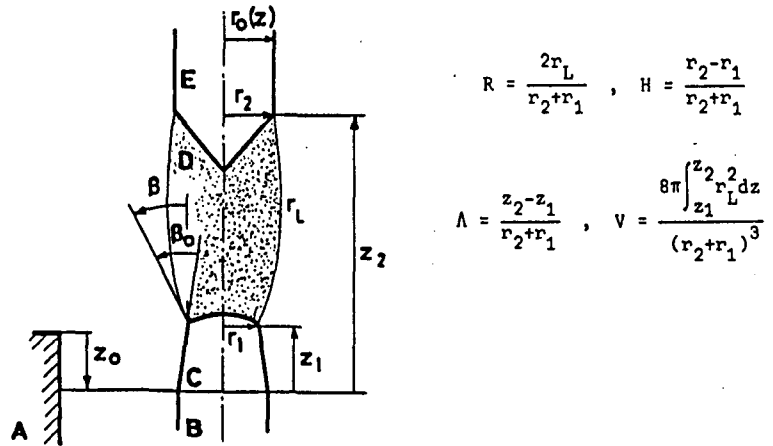


Fig. 25. Geometry and nomenclature used in the liquid bridge modeling of the floating zone growth. A furnace reference, B seed, C crystal grown, D melt, E feeding rod. All dimensions are scaled with seed radius $r_0(0)$, and the nondimensional parameters introduced are shown.

Once the three nondimensional parameters that determine the shape are measured, it is easy to look on the stability diagram for liquid bridges anchored to unequal discs [23] and see (Fig. 26) how far the stability limit is, with respect to the parameters mentioned above. However, from a

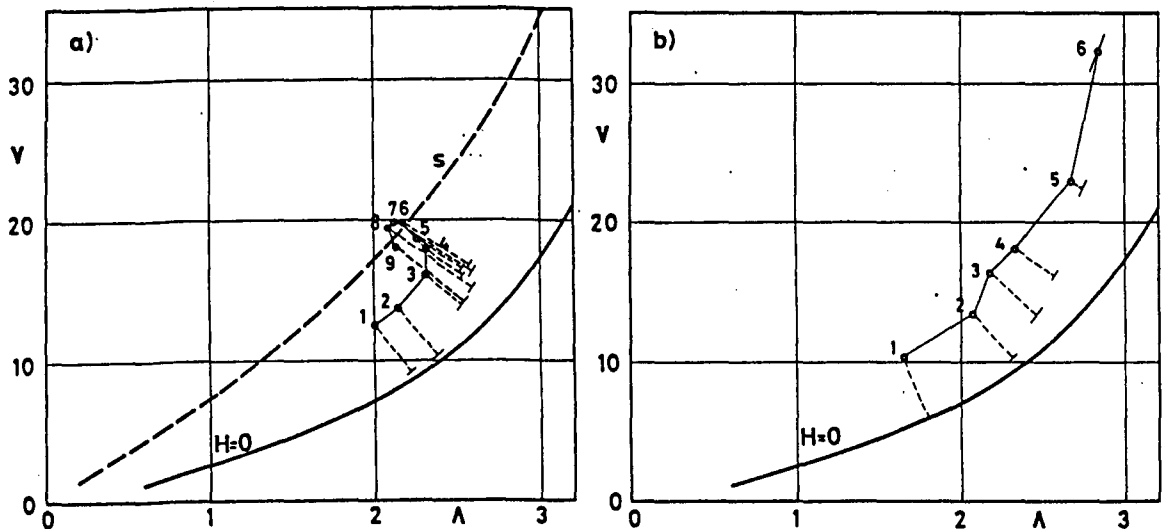


Fig. 26. Capillary stability diagram for a molten bridge. The points correspond to shapes in Fig. 5. Dashed lines indicate the stability margin (minimum distance to the stability boundary in the slenderness-volume diagram).

- Stable growth. It is seen that after shapes 3 and 4 the zone gets away from the unstable limit, approaching a point in curve s , which is the loci of cylindrical growth configurations for silicon (a barrel-shaped molten zone with 11° of bulging that moves along a cylindrical rod).
- Growth with bridge disruption. It is seen how the last shape in Fig. 21b was unstable (because of the smallness of the sample, 3.8 mm of diameter, the breaking is instantaneous).

practical point of view, what matters is the stability limits with respect to the directly controlled inputs: furnace power and pulling laws, which is a much more involved task.

The main lesson from liquid bridge theory is that the sequence of molten shapes during growth can be predicted as function of the position of the fronts and, if the small difference in density is accounted for, the volume of immersed solid tips. Thus, if a thermal analysis of furnace and rod could model these three parameter as functions of the heating and pulling laws, the behaviour of the floating zone should be entirely predictable and, consequently programed to a better advantage.

The geometry used is sketched in Fig. 25. All dimensions are scaled with the radius of the first resolidified rod section. If, for the sake of clarity, the difference between the density of liquid and solid silicon (the latter 8% larger) is neglected, the sequence of molten shapes during growth $r_L(z,t)$ is determined by knowing the initial rod shape $r_0(z)$ and the movement of the fronts: $z_1(t)$ and $z_2(t)$.

The procedure is as follows. From initial conditions, the liquid free surface is known. From that, resolidification should proceed with a constant receding angle of $\beta_0 = 11^\circ$ from the liquid free surface, thus, diminishing the solidification radius and displacing some volume v_{dis} from the initial rod towards the molten bridge (ahead of the solidification front). The liquid bridge then tends to get a barrel shape and thus, if it does not gets destabilized in the way, the angle at the border will increase restoring the solidification front radius to that of the original rod. In mathematical form:

$$dz_1/dt = f_1(t) \quad (22)$$

$$dz_2/dt = f_2(t) \quad (23)$$

$$dr_1/dt = (dz_1/dt) \cdot \tan(\beta - \beta_0) \quad (24)$$

$$dv_{dis}/dt = \pi [r_0^2(z_1) - r_1^2] \cdot (dz_1/dt) \quad (25)$$

that can easily be integrated with a standard Runge-Kutta routine, once the initial conditions $z_1=0$, $z_2=z_2(0)$, $r_1=r_1(0)=r_0(0)$, $v_{dis}=0$ are fixed, and β is expressed as a function of the variables, as explained below.

To this aim, a further simplification is now introduced: the liquid bridge shape is assume not to deviate too much from a cylinder so that the handy linear approximation:

$$R^2(z,H,\Lambda,V) = 1 + \frac{V-2\pi\Lambda}{2\pi\Lambda} \frac{\cos Z - \cos \Lambda}{\frac{\sin \Lambda}{\Lambda} - \cos \Lambda} + 2H \frac{\sin Z}{\sin \Lambda} + H^2 \frac{\frac{\sin \Lambda}{\Lambda} - \cos Z}{\frac{\sin \Lambda}{\Lambda} - \cos \Lambda} \quad (26)$$

is valid. Here, a local scale is used for the shape such that it goes from $-\Lambda$ to $+\Lambda$, with $R(-\Lambda)=1-H$, $R(+\Lambda)=1+H$, Λ being the slenderness and $V=\pi R^2 dZ$ the straight volume between ends (including immersed solid tips). These local parameters are related to the growth ones by

$$H = (r_0(z_2) - r_1) / (r_0(z_2) + r_1) \quad (27)$$

$$\Lambda = (z_2 - z_1) / (r_0(z_2) + r_1) \quad (28)$$

$$V = 8 \cdot (v_{dis} + v_0(z_2) - v_0(z_1)) / (r_0(z_2) + r_1)^3 \quad (29)$$

where $v_0(z)$ is the volume of the initial rod $r_0(z)$ from 0 to z . Furthermore, $\beta_0 = 11^\circ$ and, within the linear approximation above, β is directly given by

$$\beta = \arctg \frac{\frac{2H}{\tg \Lambda} + \frac{V}{2\pi\Lambda} - 1 - H^2}{2(1-H)} \quad (30)$$

For a given furnace and initial rod, the value $z_2(t=0)$ and the two

functions $f_1(t)$ and $f_2(t)$ only depend on the heating and pulling laws imposed. Further work will be needed to build this thermal model, but the simple procedure detailed above allows one to gain much insight in the behaviour of floating zones processing. To that aim, simple trials can be run and the effects observed. Figure 27 presents the results of such a trial: the distance between solidification and melting fronts has been assumed constant and its influence on the stability of growing studied (similarly, other laws such as maintaining the molten volume, or the free surface area, etc., can be exercised). The same approach here applied to floating zones [27] has also been successfully applied to the solidification of molten drops [28].

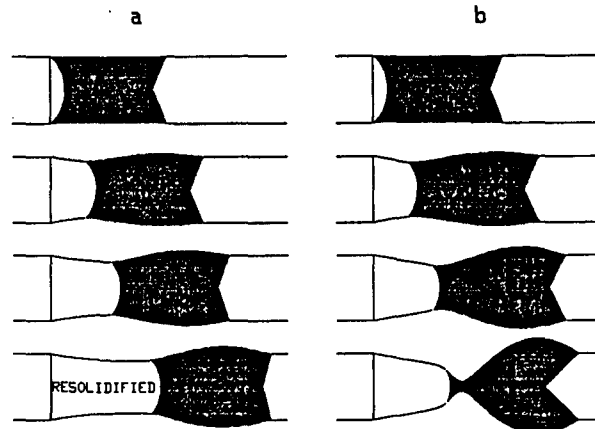


Fig. 27. Example of predicted evolution of the solidification radius, r_L , with distance from the seed, z , during floating zone processing of an initially cylindrical silicon rod. In this example, the external length of the molten bridge, $z_2 - z_1$, is assumed constant with time. Note that if $z_2 - z_1 = 3$ the crystal grows trying to recover the initial shape, whereas if $z_2 - z_1 = 4$ the growing gets unstable and the bridge breaks.

The general procedure is implemented in a computer program that works as follows:

1. Read data for material properties (solidification angle, liquid and solid density, melting temperature, specific heats, enthalpy of fusion, thermal conductivities, etc).
2. Read initial rod data (meridian section profile for an axisymmetric rod).
3. Read experiment data (pulling and heating laws as functions of time t).
4. Compute (loop) molten bridge base parameters (position of solid/melt fronts and solid volume immersed inside the stright volume, as functions of time) either from real experiments or from a thermal model (still lacking).
5. Compute liquid bridge base parameters $H(t)$, $\Lambda(t)$ and $V(t)$ from their definitions (Fig. 25).
6. Compute liquid bridge shape from base parameters by using a liquid bridge model (as Eq. 26).
7. Show predicted molten-zone evolution for the data given. Both, a rod-fixed reference frame or a furnace-fixed one may be displayed.
8. If real experiment sequence is available, compare molten shapes with predictions. In fact, this is the case here, and Fig. 28 shows the comparison for shape 6 in Fig. 24b.

The above procedure may be used advantageously to study receding angles in other similar configurations as the one shown in Fig. 29.

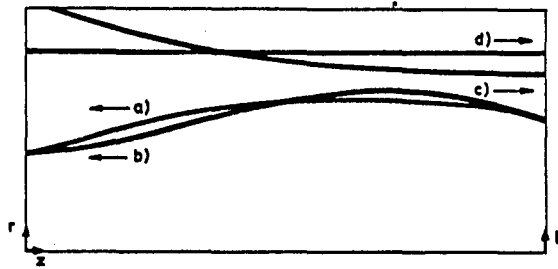


Fig. 28 Experimental a) and theoretically predicted b) shapes corresponding to stage 6 in Fig. 24b. Melt shape (after a video recording of the actual growth) appears more flattened than predicted. Its pressure profile c) should be uniform as for the theoretical shape d) (assuming constant surface tension) and it is clearly not.

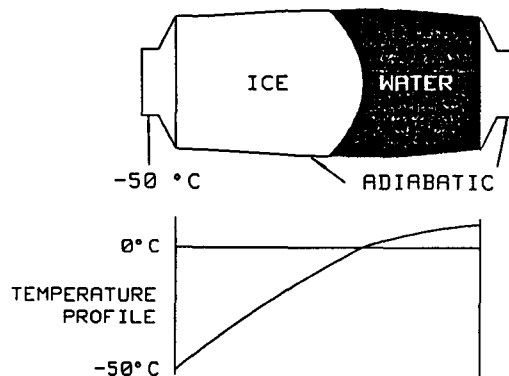


Fig. 29. An experiment proposal to study the receding angle and movement near the three-phase-line in a water column configuration.

Conclusions

A model is presented that explains the observed behaviour of molten bridges when a silicon rod is processed by the floating-zone technique under microgravity conditions. The analysis is focused in molten shape evolution, and assumes constant surface tension, no force field applied, and a given advancing angle at the solidification edge. The main results may be summarized as follows:

1. The stable evolution that occurred in the first trial of Exp. 321 aboard Spacelab is accurately predicted by the model (Fig. 26a).
2. The unstable evolution that occurred in the second trial of Exp. 321 is accounted for and accurately predicted by the model (Fig. 26b).
3. Uncertainty in shape discrimination, due to smallness of the sample, prevents a finer analysis of disturbances upon the equilibrium configurations.
4. Real bridges appear to be more flattened than expected (Fig. 28). Sizable departures of a constant pressure profile from observed shapes (pressure diminish towards the neck) need further explanation (maybe nonuniform surface tension due to temperature gradients).
5. From the history described above, the sequence of shapes may be computed, thus, the next step should be to model the thermal problem applicable to a particular type of furnace, to be able to predict the sequence of shapes directly from the heating and pulling laws.

Acknowledgement: This work is being sponsored by the Spanish Commission on Space Research.

REFERENCES

1. J. MESEGUER, L.A. MAYO, J.C. LLORENTE and A. FERNANDEZ, *J. Crystal Growth* 73, p 609, 1985.
2. I. MARTINEZ, ESA SP-222, p 31, 1984.
3. I. MARTINEZ and A. SANZ, *ESA Journal* Vol. 9, p 323, 1985.
4. I. DA RIVA and I. MARTINEZ, *Naturwissenschaften* 73, p 343, 1986.
5. J. MESEGUER, A. SANZ and J. LOPEZ, *J. Crystal Growth* (in press), 1986.
6. I. MARTINEZ and J. MESEGUER, *Norderney Symposium on Spacelab-D1 results, DFVLR (FRG)* (in press), 1986.
7. I. MARTINEZ, IAF-86-272 (to be published in *Acta Astronautica*), 1986.
8. D. LANGEBEIN, in *Materials Sciences in Space*, Springer-Verlag, 1986.
9. J. MESEGUER, *J. Fluid Mech.* 130, p 123, 1983.
10. W.G. PFANN, *J. Metals* 4, 1952.
11. A. EYER, R. NITSHE and H. ZIMMERMANN, *J. Crystal Growth* 47, p 219, 1979.
12. A. EYER, B.D. KOLBESEN and R. NITSHE, *J. Crystal Growth* 57, p 145, 1982
13. R. SCHONHOLZ, R. DIAN and R. NITSHE, *J. Crystal Growth* 72, p 72, 1985.
14. G. NAGEL and K.W. BENZ, *Adv. in Space Research* 4.5, p 23, 1984.
15. A. EYER, H. LEISTE and R. NITSHE, ESA SP-222, p 173, 1984.
16. A. EYER, H. LEISTE and R. NITSHE, *J. Crystal Growth* (submitted).
17. T. SUREK and B. CHALMERS, *J. Crystal Growth* 29, p 1, 1975.
18. A. EYER, H. LEISTE and R. NITSHE, *J. Crystal Growth* 71, p 173, 1985.
19. I. MARTINEZ, *COSPAR Space Research XVIII*, p 519, 1978.
20. I. DA RIVA and I. MARTINEZ, ESA SP-142, p 67, 1979.
21. I. MARTINEZ and D. RIVAS, *Acta Astronautica* 9, p 339, 1982.
22. A. SANZ and I. MARTINEZ, *J. Colloid Interf. Sci.* 93, p 235, 1983
23. I. MARTINEZ, ESA SP-191, p 267, 1983.
24. J. MESEGUER, *J. Crystal Growth* 67, p 141, 1984.
25. J. MESEGUER, ESA SP-222, p 297, 1984.
26. I. MARTINEZ and J.M. PERALES, *J. Crystal Growth* (in press), 1986.
27. I. MARTINEZ and A. EYER, *J. Crystal Growth* 75, p535, 1986.
28. A. SANZ, *J. Crystal Growth* 74, p 642, 1986.